

Scintillation Properties of Ce³⁺/Tb³⁺ Co-doped Oxyfluoride Glass with the Exploration of Imaging Application^①

CHEN Da-Yi^{a, b} LI Yan^{b, c} WU Yi-Heng^{a, b} WANG Zhi-Lin^{a, b}
WANG Shuai-Hua^{b②} SU Qing^d ZHANG Bi-Sheng^d
ZENG Qing-You^d WU Shao-Fan^{b②}

^a (University of Chinese Academy of Sciences, Chinese Academy of Sciences, Beijing 100039, China)

^b (Key Laboratory of Optoelectronic Materials Chemistry and Physics, Collaborative Innovation Center for Optoelectronic Semiconductors and Efficient Devices, Fujian Institute of Research on the Structure of Matter, Chinese Academy of Sciences, Fuzhou 350002, China)

^c (College of Chemistry, Fuzhou University, Fuzhou 350108, China)

^d (Fujian Luhai Engineering Investigation & Designing Company, Fuzhou 350007, China)

ABSTRACT Scintillator is a material that converts high-energy rays into visible light, and has great applications in high-energy physics, medical imaging, and security inspections. As a type of scintillator, scintillation glass has the advantages of low cost, high stability, controllable shape, and ability to be prepared on a large scale. In this paper, a traditional fusion quenching method was used to prepare a cerium-terbium co-doped glass. The green characteristic light of Tb ion was observed at 543 nm. Moreover, through the doping sensitization of Ce ions, the luminescence of Tb was successfully enhanced. The material has high X-ray response sensitivity, complete stability and strong X-ray emission intensity. We use a simple X-ray imaging platform for imaging, and the results show that our glass has a spatial resolution of 7.0 lp/mm.

Keywords: scintillators, light yield, glass, X-ray imaging, luminescence;

DOI: 10.14102/j.cnki.0254-5861.2011-3146

1 INTRODUCTION

Scintillator is an energy conversion material that can convert signals that are not easily detectable, such as high-energy ions (α particles, neutrons, protons, etc.) and high-energy rays (X-rays, β -rays), into detectable signals^[1-4]. There are many types of scintillators, mainly scintillation of crystals, ceramics and glasses. Compared with scintillation of crystals and ceramics, scintillation glass has the characteristics of simple preparation process, low cost, good thermal stability, high transparency, and the ability to prepare bulk detectors^[5, 6]. At present, scintillation glass is gradually becoming a research hotspot due to its potentiality of applications in high-energy physics, medical imaging, border

security, and astrophysics^[7, 8].

Scintillation glass generally takes rare earth ions as its luminescence center, and common ones include^[9-13] Ce³⁺, Tb³⁺, Sm³⁺, Dy³⁺, etc. There are many studies on Ce³⁺ and Tb³⁺ ion single-doped glass^[14-16], but few reports on the Ce³⁺/Tb³⁺ co-doped scintillation glass. The glass matrix of scintillation glass usually includes silicate, borate, germanate, and phosphate systems^[17, 18]. As the most widely studied glass, silicate always has the characteristics of strong chemical stability and high transparency, but its low density and low X-ray cut-off ability will limit its application in scintillation^[19]. Therefore, we can increase the density of glass by introducing heavy metal ions. This article introduces gadolinium and gallium as heavy ions into the glass matrix to increase the

Received 22 February 2021; accepted 15 April 2021

① The work was supported by the National Natural Science Foundation of China (No. 22075284, 51872287 and U2030118), Equipment Pre-research Foundation Project of China (No. 61409220309), and the Financial Support of Fujian Province under Grant 2018Y024 and Grant 2019T3011, and supported by the Open-Foundation of Key Laboratory of Laser Device Technology, China North Industries Group Corporation Limited

② Corresponding authors. E-mails: shwang@fjirsm.ac.cn and sfwu@fjirsm.ac.cn

glass density. Oxyfluoride glass is the current research popular direction, mainly because it combines the high mechanical strength of oxide glass and the low generation energy of fluoride glass. Not only the tolerance of rare earth ions is high, but the chemical composition ratio can be adjusted in a wide range.

Thence, this article takes $\text{Ce}^{3+}/\text{Tb}^{3+}$ co-doped oxyfluoride scintillation glass as the research target to explore its scintillation performance. Experiments indicated that cerium ions can sensitize the luminescence of terbium ions. The XEL strength of $\text{Ce}^{3+}/\text{Tb}^{3+}$ co-doped scintillation glass is 1.8 times that of Tb^{3+} ion single-doped glass. For the X-ray imaging research, there have been reports on the imaging of crystals^[20-23], but almost no reports of imaging of glass are found. In order to image the cerium-terbium co-doped glass, we independently built a simple X-ray imaging platform. The results showed that at a dose rate of 42.29 mGys^{-1} , the resolution reached 7.0 lp/mm of the spatial resolution card. Similarly, the corresponding sensitivity of the glass to X-ray was tested, and the results showed that the sensitivity of $\text{Ce}^{3+}/\text{Tb}^{3+}$ co-doped scintillation glass is 1.7 times that of the BGO crystal. This certifies that the cerium-terbium co-doped glass we prepared has high resolution and corresponding radiation sensitivity, which can be applied in practical work.

2 EXPERIMENTAL

2.1 Materials and instruments

Silicon dioxide (SiO_2 , 99%), aluminium oxide (Al_2O_3 , 99%), strontium fluoride (SrF_2 , 99%), diantimony trioxide (Sb_2O_3 , 99%), gadolinium oxide (Ga_2O_3 , 99.99%), gadolinium fluoride (GdF_3 , 99.99%), tetraterbium heptaoxide (Tb_4O_7 , 99.995%)

and cerium oxide (CeO_2 , 99.995%) were all purchased from Aladdin.

2.2 Synthesis of oxyfluoride glass

The oxyfluoride glasses were admixed through a conventional melting-quenching method, as shown in Fig. 1a. The raw materials were all accurately weighed according to the molar ratio firstly (The formula is shown in Table 1). Then they were placed in an agate mortar, ground and mixed thoroughly for half an hour. Subsequently, the well mixed powder was transferred to a covered alumina crucible and melted at 1500°C for 30 min in the box furnace. The melt mixture was poured into a preheated iron mold, annealed rapidly in a muffle furnace at 400°C for 4 hours to relieve thermal stress, and cooled naturally to room temperature to form bulk glass. With cutting and polishing, a series of oxyfluoride glass samples with terbium ion doping and Ce-terbium ion co-doping were all available, which were $15\text{mm} \times 15\text{mm}$ in size. At last, after naming the host glass as HG, the glass doped with tetraterbium heptaoxide as T, the glass doped with cerium oxide as C, and the glass co-doped with cerium oxide and tetraterbium heptaoxide as CT, we went further optical performance test.

Fig. 1b is a picture of the scintillation glass sample prepared in the experiment under sunlight and X-ray with a dose rate of 42.29 mGys^{-1} . It can be seen from the figure that due to the difference in doping concentration and composition, the transmittance of glass under natural light has changed, but basically retains a very high transmittance, while the luminescence under radiation changes greatly. The matrix glass hardly emits light, but cerium single-doped glass samples emit faint blue light and cerium-terbium double-doped glass samples can emit extremely bright green light.

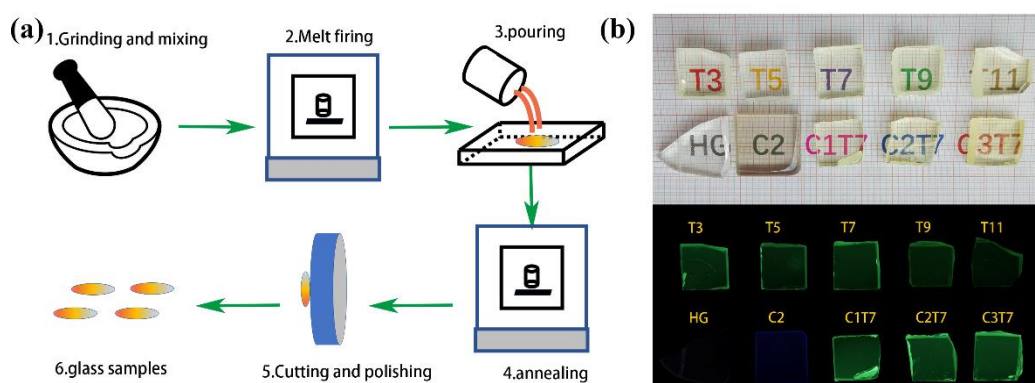


Fig. 1. (a) Picture of flow chart of making glass experiment, (b) Picture of glass sample under sunlight and X-ray irradiation

Table 1. Composition of Oxyfluoride Glass Samples

45SiO ₂ -28Ga ₂ O ₃ -6Al ₂ O ₃ -0.5Sb ₂ O ₃ -14.5SrF ₂ -6GdF ₃ -xTb ₄ O ₇ -yCeO ₂									
Doping concentration (mol%)									
Sample	HG	T3	T5	T7	T9	T11	C1T7	C2T7	C3T7
x	1	3	5	7	9	11	7	7	7
y	0	0	0	0	0	0	1	2	3

2.3 Materials and instruments

The density test was carried out using electronic density meter (DX-120C). The XRD characterization was measured over the scanning range of 10~80 ° (2θ) by a MiniFlex600 X-ray diffractometer at room temperature. The thermal stability analysis experiment of oxyfluoride glass samples was measured by Synchronous thermal analyzer (STA4493) heated from 50 to 900 °C at a heating rate of 10 °C/min under air atmosphere. The UV-Vis absorption spectra were probed by UV-Vis NIR spectrophotometer (Lambda 950). Photoluminescence (PL) spectra were examined to seek excitation and emission spectra using an FLS 1000 spectrometer, which were excited by xenon lamp (500 W). The fluorescence lifetime test was also carried out by using the FLS 1000 spectrometer, but different in the excitation source, the later was excited by a Microsecond lamp. X-ray excitation spectroscopy was tested by X-ray source (MagProTUB0014).

3 RESULTS AND DISCUSSION

3.1 Density

The results of density measurement are shown in Table 1, from which we can see that the density of all glass sample is above 4.2 g/cm³, the minimum is 4.281 g/cm³ for the matrix glass and the maximum is 4.762 for the T11 sample. Obviously, the density of glass sample increases with increasing the doping concentration of cerium oxide and tetraterbium heptaoxide because rare earth ion has higher atomic number and larger ion radius. High density helps increase the absorption coefficient, thereby reducing the radiation length of the scintillator, which is an important parameter for evaluating scintillator performance. The lower the radiation length, the smaller the size of scintillator required, and the smaller the cost and detector volume. The principle is as follows:

$$I = I_0 e^{-\mu d}$$

Where I is the energy passing through the scintillator, d is the thickness of the scintillator, and μ is the absorption coefficient of the scintillator for high-energy rays or high-energy particles.

Table 2. Density Table of Glass Samples

Sample	CeO ₂ (mol%)	Tb ₄ O ₇ (mol%)	Density (g/cm ³)
HG	0	0	4.281
C2	2	0	4.305
T3	0	3	4.340
T5	0	5	4.506
T7	0	7	4.503
T9	0	9	4.628
T11	0	11	4.762
C1T7	1	7	4.445
C2T7	2	7	4.452
C3T7	3	7	4.489

3.2 UV-Vis absorption spectra

Fig. 2 elaborates the absorption UV-Vis spectra of host glass (HG), Ce³⁺ doped (C2), Tb³⁺ doped (T7) and Ce³⁺/Tb³⁺ co-doped (CT) transparent glass samples in the range of 300~700 nm. In this figure, all samples exhibit high transparency from 400 to 700 nm. It can be seen from the figure that as the doping concentration of rare earth compounds

increases, the UV absorption edge shrinks from 343 to 383 nm. For the T7 sample curve, absorption peaks are observed at 350, 369, 378 and 484 nm, which represent ⁷F₆→⁵L₉, ⁵L₁₀, ⁵D₃ and ⁵D₄ of Tb³⁺ ions respectively. The same peak at 484 nm can be observed in the CT sample, but those at 351, 368, and 378 nm disappeared, which may be due to the influence of cerium ions.

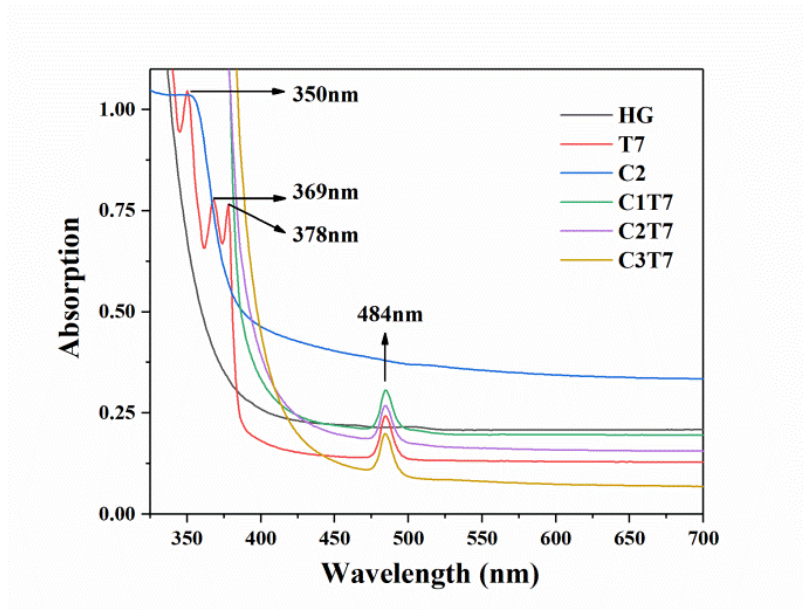


Fig. 2. UV-Vis spectra of host glass (HG), Ce^{3+} doped (C2), Tb^{3+} doped (T7) and $\text{Ce}^{3+}/\text{Tb}^{3+}$ co-doped (CT) transparent glass samples

3.3 X-ray diffraction pattern

The X-ray diffraction patterns of glass samples HG, C2, T7, and C2T7 are located in Fig. 3. Clearly, there is no evident

sharp peak in the whole patterns, and we can find a broad peak between 15° and 35° . That will confirm the amorphous nature of the inorganic salt of the sample we prepared.

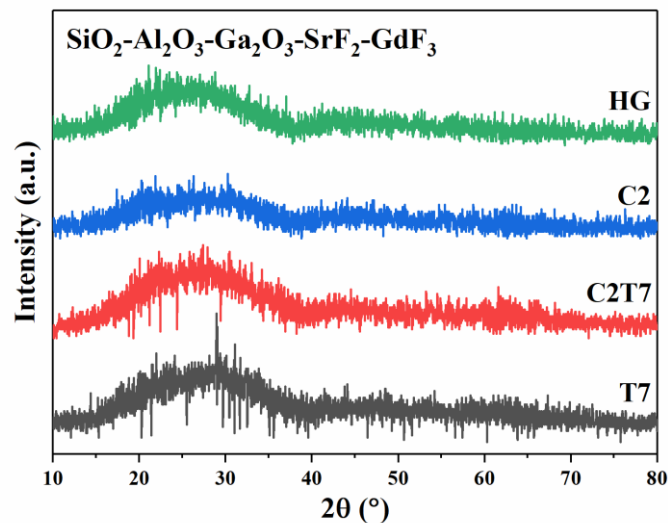


Fig. 3. XRD patterns of host glass (HG), Ce^{3+} doped (C2), Tb^{3+} doped (T7), and $\text{Ce}^{3+}/\text{Tb}^{3+}$ co-doped (C2T7) samples

3.4 TG/DTA

Fig. 4 shows the TG/DTA chart of $\text{Ce}^{3+}/\text{Tb}^{3+}$ co-doped C2T7 glass sample. It can be seen from the figure that in the range of $100\sim 900^\circ\text{C}$, the glass almost does not lose weight,

indicating that the glass has good thermal stability and can well meet the work needs of scintillating materials in high-temperature environments.

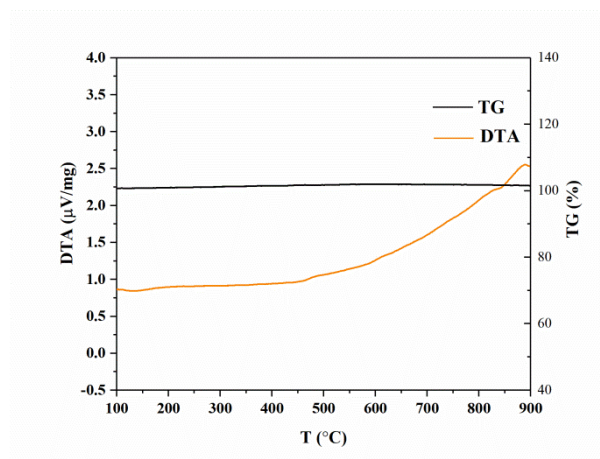


Fig. 4. TG/DTA chart of $\text{Ce}^{3+}/\text{Tb}^{3+}$ co-doped C2T7 glass sample

3.5 Photoluminescence spectroscopy

Fig. 5 exhibits the fluorescence excitation and emission spectra of host glass (HG), Tb^{3+} doped glass (T7), Ce^{3+} doped glass and $\text{Ce}^{3+}/\text{Tb}^{3+}$ co-doped glass (C2T7) samples. As can be seen from Fig. 5a, the main excitation peaks of the HG sample falling at 273, 307, and 312 nm represent $^8S_{7/2} \rightarrow ^6I_J$, $^6P_{5/2}$, and $^6P_{7/2}$ of Gd^{3+} ion, separately; the main emission peaks of the HG sample at 612 nm may be the result of defect state light emission. Fig. 5b shows the excitation peaks of 301, 317, 340, 351, 368, 378 and 484 nm, which correspond to $^7F_6 \rightarrow ^5H_6$, 5H_7 , 5L_8 , 5L_9 , $^5L_{10}$, 5D_3 and 5D_4 of Tb^{3+} ions, respectively. Similarly, the main emission peaks of T7 sample at 489, 543, 583 and 621 nm exactly match $^5D_4 \rightarrow ^7F_6$, 7F_5 , 7F_4 and 7F_3 . Furthermore, the

excitation wavelength of the strongest emission peak is 351 nm, and the emission wavelength of the strongest excitation peak is 543 nm. The excitation peaks of the excitation spectra of the C2 sample are two broad peaks of 270 and 302 nm, corresponding to $^2F_{2/5}$ and $^2F_{2/7} \rightarrow ^5D$, and $^2F_{2/5}$ and $^2F_{2/7}$ belonging to the $4f$ energy level spin-orbital split. And there is only one broad peak of emission spectra of C2 sample at 381 nm, which matching electric dipole allows the transition of $5d \rightarrow 4f$. In Fig. 5d, the excitation peaks are only 301, 351, 369, 378 and 484 nm, however 317 and 340 nm vanish because they are covered by the excitation peak of Ce^{3+} ion at 301 nm of $4f \rightarrow 5d$. While compared with the T7 sample, the emission peak position of the C2T7 sample has not changed.

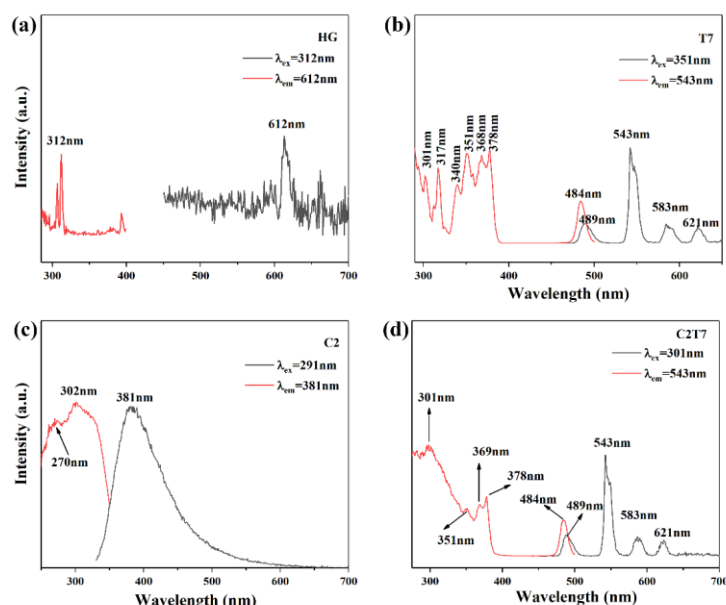


Fig. 5. Excitation and emission spectra of (a) host glass (HG), (b) Tb^{3+} doped glass (T7) (c) Ce^{3+} doped glass (d) $\text{Ce}^{3+}/\text{Tb}^{3+}$ co-doped glass (C2T7) samples

As Fig. 6 shows, the X-ray excited optical luminescence intensity increases with the growth of Tb³⁺ doping concentration, and reaches the maximum when the concentration of Tb₄O₇ is 4%. But the emission intensity of T9 and T11 samples decreased, which may be the result of concentration quenching. Similarly, the same phenomenon can be observed in the emission spectrum of Ce³⁺/Tb³⁺ co-doped glass samples. The emission intensity first increases with the doping concentration, the C2T7 sample is the largest, and then decreases. They are also due to the concentration quenching effect. It is worth noting that the emission intensity of the cerium-terbium co-doped samples is significantly enhanced compared to the samples doped with cerium ion alone, because the Ce³⁺ ion can sensitize the luminescence of Tb³⁺. According to the previously measured excitation peaks of the C2T7 samples in Fig. 5d, we measured the emission spectra of the C2T7 samples at different excitation wavelengths and found that the excitation spectrum intensity was the strongest at 301 nm. However, the strongest excitation wavelength of T7 glass sample is 351 nm. The reason is that the excitation peak of Ce³⁺ ion at 301 nm, attributed to the 4f→5d electronic transition, is superimposed with the excitation peak of ⁷F₆→⁵H₆ of Tb³⁺ at 301 nm and thus enhances the emission of Tb³⁺.

Fluorescence decay curve of Ce³⁺/Tb³⁺ co-doped (C2T7),

Ce³⁺ doped (C2), and Tb³⁺ doped (T5) samples are placed at Fig. 7. Fluorescence lifetime refers to the average residence time of a molecule in the excited state before it returns to the ground state after being excited by a light pulse. The fluorescent molecule in the excited state emits fluorescence and releases energy during the process of de-excited to the ground state. The decay of the fluorescence intensity of the excited state fluorophore can be expressed as a single exponential function by mathematical formula:

$$I(t) = I_0 \exp\left(-\frac{t}{\tau}\right)$$

Among them, $I(t)$ is the intensity measured at time t after the sample is excited by the light pulse; I_0 is the intensity at $t = 0$; τ is the average fluorescence lifetime and is the characteristic value of the molecule, defined as t The time required for the fluorescence intensity to decay to $1/e$ of the initial value I_0 . According to this principle, we can calculate: The fluorescence lifetime of the C2T7 sample under excitation at 301 nm and emission at 543 nm is 2.26 ms. The fluorescence lifetime of the C2 sample upon 291 nm excitation and 381 nm emission is 1.42 μ s. The fluorescence lifetime of the T7 sample under the conditions of excitation (301 nm) and emission (543 nm) is 2.00 ms. This composite Tb³⁺ ion has a slower decay characteristic than Ce³⁺ ion.

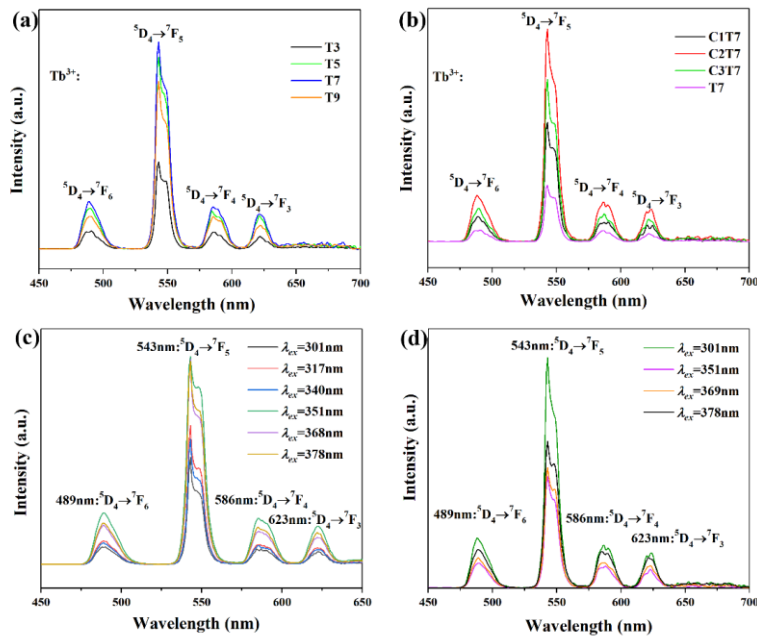


Fig. 6. Emission spectrum of series doping concentration of (a) Tb³⁺ doped (T) glass samples, (b) Ce³⁺/Tb³⁺ co-doped (CT) glass samples; emission spectra under different excitation wavelengths of (c) T7 glass sample, (d) C2T7 glass sample

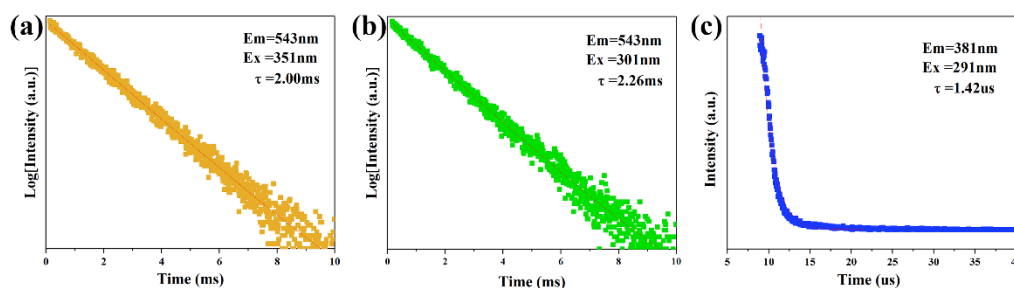


Fig. 7. Fluorescence decay curve of (a) Tb^{3+} doped (T7), (b) $\text{Ce}^{3+}/\text{Tb}^{3+}$ co-doped (C2T7), (c) Ce^{3+} doped (C2) glass samples

3.6 X-ray luminescence spectra

Fig. 8a illustrates the X-ray luminescence spectra of Tb^{3+} doped glass samples, from which we can see the position of the peak is consistent with that of the PL spectra. Meanwhile, the intensity of ray emission increases with raising the Tb^{3+} doping concentration. The strongest is the T7 sample, which is also consistent with the PL spectrum. Fig. 8c clearly compares the X-ray emission intensity of different samples with BGO crystals. It is not difficult to find that $\text{Ce}^{3+}/\text{Tb}^{3+}$ co-doped glass sample has a significant increase in ray intensity compared to the Tb^{3+} doped one, with the peak intensity increased by 0.8 times. In addition, the peak intensity of the C2T7 sample is 1.97 times that of BGO crystal but the peak integrated area is only 0.32 times that of BGO crystal. Fig. 8c shows the

sensitivity curves of C2T7 samples, and BGO and LYSO crystals. As the X-ray dose rate increases, the X-ray intensity of them all increases linearly. The comparison of the slope K is $K_{\text{LYSO}} > K_{\text{C2T7}} > K_{\text{BGO}}$. Through the fitting results, the values of K are 4.647, 1.816 and 1.064, respectively. The fitting equations are $y_{\text{LYSO}} = 2767 + 4.647x$, $y_{\text{C2T7}} = -1517 + 1.816x$, and $y_{\text{BGO}} = -1287 + 1.064x$, respectively. Therefore, our cerium-terbium double-doped glass has higher X-ray sensitivity than BGO crystals. As we all know, the higher the sensitivity of the scintillation material, the higher the imaging resolution, the smaller the radiation dose required, and the less radiation damage to human body. Therefore, our cerium-terbium double-doped glass will be a scintillating glass material with high sensitivity and high ray response.

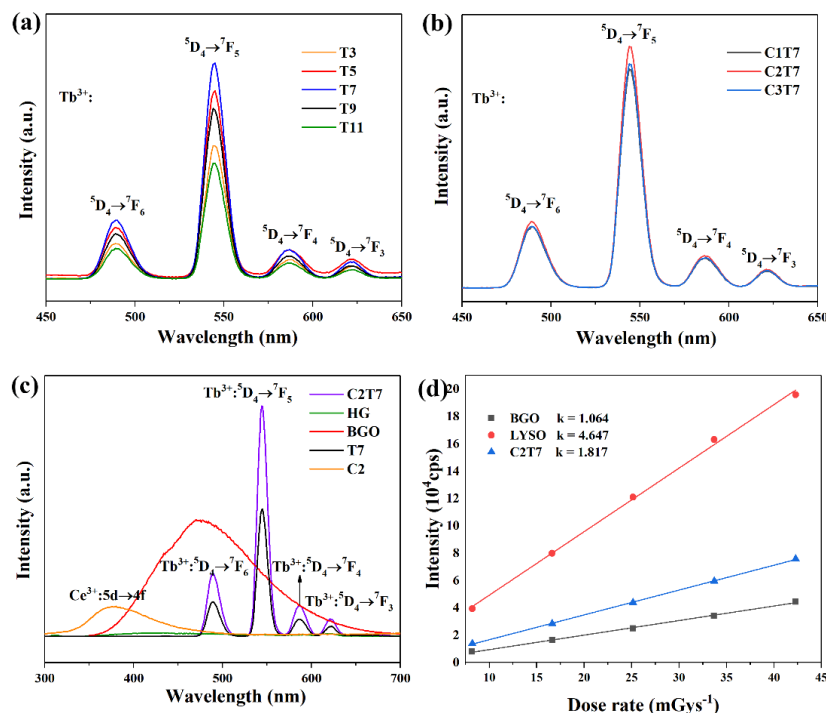


Fig. 8. XEL spectra at a dose rate of 42.29 mGys^{-1} of (a) Tb^{3+} single-doped glass samples, (b) $\text{Ce}^{3+}/\text{Tb}^{3+}$ co-doped glass samples, (c) HG, C2, T7 and C2T7 glass samples and BGO crystals; (d) XEL intensity at different radiation dose rates of BGO crystals, LYSO crystals and C2T7 glass sample

3.7 X-ray imaging

Fig. 9a illustrates the schematic diagram of the principle of X-ray imaging. We built an uncomplicated X-ray imaging platform with ray source (MagProTUB0014), imaging objects, C2T7 glass, digital cameras and laptops. X-ray imaging is mainly based on the ability of scintillating materials to transit from the valence band to the conduction band under the radiation of high-energy rays to form electron-to-face pairs. The electrons recombine with the mixture and release energy in the form of photons. Traditional scintillation detectors are mainly composed of scintillators, light collection components and photoelectric conversion devices. The horizontal lines are arranged. The role of the lead box is to conduct radiation to prevent the damage to human body, also avoiding the influence of natural light on the experiment.

First the ray hits the object, then passes through the C2T7 glass, and finally the camera captures and takes a

video. Because different components in the object have inconsistent ray cut-off capabilities, the intensity of the rays at different positions after passing through the object is different, which causes the luminous brightness of the scintillation glass to change, so it can be imaged. At the top of Fig. 9b is the Type 81 spatial resolution test card, which reflects the inherent spatial resolution of X-ray imaging, and its X-ray imaging picture at a dose rate of 42.29 mGy s⁻¹. As can be seen from Fig. 9b, our scintillation glass imaging resolution has reached 7.0 lp/mm. At the same time, we also took the common plastic wires to do imaging experiments, and the results of the imaging photo can clearly see the internal metal wires wrapped in the plastic shell, which indicates that our scintillation glass has excellent spatial resolution. In addition, glass has the characteristics of easy availability, short preparation cycle, and large area glass preparation. Therefore, our scintillation glass will have great potential as a large area scintillation detector.

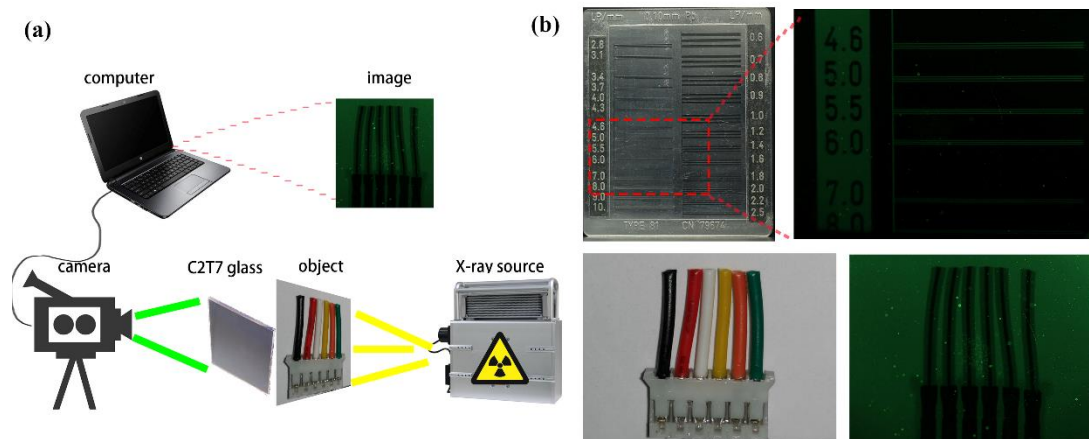


Fig. 9. (a) Schematic diagram of X-ray excitation imaging, (b) objects in daylight and images imaged under X-ray irradiation

4 CONCLUSION

In summary, we prepared the oxyfluoride scintillation glass co-doped with cerium and terbium by the melt quenching method, which had high transmittance, high thermal stability and high density. Through the doping of cerium ions, the characteristic emission peak of terbium at 543 nm is significantly enhanced by 0.8 times. Moreover, the X-ray emission intensity of Ce³⁺/Tb³⁺ co-doped glass (C2T7) is 1.97

times that of BGO crystal, and the X-ray response sensitivity of C2T7 sample is 1.70 times that of BGO crystal. Furthermore, we used the prepared cerium-terbium co-doped scintillation glass for X-ray imaging, and the results showed that our glass has outstanding spatial resolution of 7.0 lp/mm at a dose rate of 42.29 mGy s⁻¹. It is expected to be a candidate material for large-area scintillation detectors. In the future, we will further conduct research on the preparation of detector devices.

REFERENCES

- (1) Zanella, G.; Zannoni, R.; Dalligna, R. Nuclear instruments and methods in physics research section a: accelerators, spectrometers, detectors and associated equipment. *Nucl. Instr. Meth. A* **1994**, 345, 198–201.
- (2) Anderson, D. F. Properties of the high-density scintillator cerium fluoride. *IEEE T. Nucl. Sci.* **1989**, 36, 137–140.

- (3) Blasse, G. Scintillator materials. *Chem. Mater.* **1994**, 6, 1465–1475.
- (4) Murray, R. B.; Meyer, A. Scintillation response of activated inorganic crystals to various charged particles. *Phys. Rev.* **1961**, 122, 815–826.
- (5) Liu, S.; Zheng, S. P.; Tang, C. M. Photoluminescence and radio luminescence properties of Yb³⁺-doped silica glass. *Mater. Lett.* **2015**, 144, 43–45.
- (6) Nguyen, L. Q.; Gabella, G.; Goldblum, B. L.; Laplace, T. A.; Carlson, J. S.; Brubaker, E.; Feng, P. L. Boron-loaded organic glass scintillators. *Nucl. Instrum. Meth. A* **2021**, 988, 164898–7.
- (7) Ortega-Alfaro, M. C.; Hernández, N.; Cerna, I.; López-Cortés, J. G.; Gómez, E.; Toscano, R. A.; Alvarez-Toledano, C. Novel dinuclear iron (0) complexes from α,β -unsaturated ketones β -positioned with sulfide and sulfoxide groups. *J. Organomet. Chem.* **2004**, 689, 885–893.
- (8) Lecoq, P. On the stabilization of Ce, Tb, and Eu ions with different oxidation states in silica based glasses. *J. Alloy. Compd.* **2016**, 809, 130–139.
- (9) Ronda, C.; Wiczeorek, H.; Khanin, V.; Rodnyi, P. Review—scintillators for medical imaging: a tutorial overview. *Ecs. J. Solid. State. Sc.* **2016**, 5, 3121–3125.
- (10) Wantana, N.; Kaewnuam, E.; Kim, H. J. X-ray/proton and photoluminescence behaviors of Sm³⁺ doped high density tungsten gadolinium borate scintillating glass. *J. Alloy. Compd.* **2020**, 849, 156574–8.
- (11) Lecoq, P. Development of new scintillators for medical applications. *Nucl. Instrum. Meth. A* **2016**, 809, 130–139.
- (12) Lecoq, P.; Gektin, A.; Korzhik, M. *Inorganic Scintillators for Detecting Systems*. Springer International Publishing, Switzerland, **2017**, p1–408.
- (13) Kawano, N.; Kawaguchi, N.; Okada, G. Scintillation and dosimetric properties of Ce-doped strontium aluminoborate glasses. *J. Non-Cryst. Solids* **2017**, 030, 0022–3093.
- (14) Saidi, K.; Dammak, M. Crystal structure, optical spectroscopy and energy transfer properties in NaZnPO₄:Ce³⁺, Tb³⁺ phosphors for UV-based LEDs. *RSC Adv.* **2020**, 37, 21867–21875.
- (15) Yi, Z.; Lu, W.; Qian, C.; Zeng, T.; Yin, L. Urchin-like Ce/Tb co-doped GdPO₄ hollow spheres for in vivo luminescence/X-ray bioimaging and drug delivery. *Biomater. Sci.* **2014**, 10, 1404–1411.
- (16) Zhang, W.; Hua, R.; Qi, X.; Zhao, J.; Qin, L.; Liu, T. Photoluminescence properties and energy transfer of Ce³⁺–Tb³⁺ co-doped SrAlF₅ nanorods by a hydrothermal method. *CrystEngComm.* **2017**, 19, 5214–5222.
- (17) Liang, C.; Gong, X. H.; Huang, J. H. Preparation and spectroscopic properties of Pr³⁺-doped transparent glass-ceramic containing LiYF₄ nanocrystals. *Chin. J. Struct. Chem.* **2017**, 36, 614–620.
- (18) Zhang, H. D.; Wang, S. H.; Wu, S. F. A new copper coordination polymer with magnetic property based on 3-(1,2,4-triazol-1-yl) benzoic acid. *Chin. J. Struct. Chem.* **2017**, 036, 2011–1615.
- (19) Chen, J.; Wang, S. H.; Zhang, H. D. Crystal structure and luminescence with relative principles calculation of a new one-dimensional Zn(II) coordination polymer. *Chin. J. Struct. Chem.* **2017**, 36, 711–715.
- (20) Liang, J. X.; Xin, S. L.; Qing, Q. H. Highly efficient eco-friendly X-ray scintillators based on an organic manganese halide. *Nat. Commun.* **2020**, 11, 4329–7.
- (21) Zhang, Y. H.; Sun, R. J.; Ou, X. Y. Metal halide perovskite nanosheet for X-ray high-resolution scintillation-imaging screens. *ACS Nano.* **2019**, 13, 2520–2525.
- (22) Cao, J. T.; Guo, Z.; Zhu, S. Preparation of lead-free two-dimensional-layered (C₈H₁₇NH₃)₂SnBr₄ perovskite scintillators and their application in X-ray imaging. *ACS Appl. Mater. Inter.* **2020**, 12, 19797–19804.
- (23) Qiu, Z. H.; Wang, S. H.; Wang, W. Q. Polymer composites entrapped Ce-doped LiYF₄ microcrystals for high-sensitivity X-ray scintillation and imaging. *ACS Appl. Mater. Inter.* **2020**, 12, 29835–29843.
- (24) Jin, H. H.; Dong, H. S. High-performance next-generation perovskite nanocrystal scintillator for nondestructive X-ray imaging. *Adv. Mater.* **2018**, 1801743–6.